





Cite this: *Nanoscale*, 2025, **17**, 17294

Anomalous ionic conduction in ferroelectric semiconductor junctions comprising multistate $\text{CuInP}_2\text{S}_6^\dagger$

Jiarui Liu, ^{‡a} Qiaoqiao Wang, ^{‡a} Hao Feng,^a Yongyi Wu, ^a Yan Li,^a Feiyan Hou,^a Tai Min^{*a,b} and Tao Li^{*a}

Van der Waals ferroelectric CuInP_2S_6 (CIPS) has emerged as a compelling candidate for multifunctional electronic devices, attributed to its intrinsic multiple polarization states and the coupling of these states with highly active Cu^+ ions migration. Such a "ferroionic" feature of CIPS opens a new paradigm for the next-generation multifunctional ferroelectric devices. Here, we present a comprehensive investigation of n^{++} -Si/CIPS/ MoS_2 ferroelectric semiconductor junction (FSJ) devices, focusing on the interplay between ferroelectric polarization and ionic migration. By employing high-resolution piezoresponse force microscopy and conductive atomic force microscopy imaging and spectroscopy methods, we revealed the distinctive dual and quadruple polarization states of the FSJ, which give rise to distinct memristive and rectifying electronic behaviors, respectively. The dual-polarization FSJ exhibits voltage- and frequency-dependent current–voltage hysteresis, while the quadruple-polarization FSJ achieves a rectification ratio exceeding 10^4 , which can be attributed to Cu^+ ion migration correlated with ferroelectric polarization modulation. This work establishes an effective strategy for leveraging ferroelectric-ionic coupling to achieve multifunctional device performance, paving the way for advanced electronic systems through interfacial engineering in future non-volatile memories and neuromorphic computing applications.

Received 9th May 2025,
Accepted 28th June 2025

DOI: 10.1039/d5nr01908g

rsc.li/nanoscale

Introduction

In recent years, there has been a surge of research interest in neuromorphic computing, leveraging the integrated storage and computation capabilities of memristors.^{1–3} The two-terminal ferroelectric semiconductor junction (FSJ)^{4,5} has garnered significant attention, especially with the emergence of van der Waals (vdW) ferroelectric materials. Unlike ferroelectric tunnel junctions that rely on quantum mechanical tunnelling through an ultrathin ferroelectric layer,⁶ FSJs utilize polarization-induced charge doping and do not require an ultrathin ferroelectric layer,⁵ thereby being less susceptible to depolarization fields. Furthermore, FSJs also feature simplified fabrication processes, cost-effectiveness, and structural configur-

ations that closely mimic biological neurons, all of which contribute to their enhanced suitability for vertical integration in advanced electronic systems.^{4,5} Significant potential is presented from emerging two-dimensional (2D) ferroelectric materials and their vdW heterostructures for applications in optoelectronic synapses,^{7–10} quantum tunneling,^{11–13} and neuromorphic computing.^{14–16} Among these 2D ferroelectrics, the ferroionic^{17–20} CuInP_2S_6 (CIPS) exhibits unique intrinsic multiple ferroelectric polarization states^{21,22} and concurrent ion migration, which underscore its significant potential for application in advanced multifunctional electronic information systems.

In CIPS-based electronic devices, the contribution of controllable Cu^+ ions migration and interfacial Schottky barrier has been proposed to control the current flow and device performance.²³ Additionally, the polarization switching of CIPS can influence the electronic transport and photoluminescent behaviour of MoS_2 .^{24,25} In addition, the formation and rupture of Ag conduction filaments have been reported to be the main cause of the switching behaviour in the Ag/CIPS/Au memristor.²⁶ Furthermore, the fundamental functions of synapses, including pulse facilitation, short-term plasticity, and long-term plasticity, have been emulated through the long-range migration of Cu^+ ions.^{7,27–30} All these studies have emphasized

^aCenter for Spintronics and Quantum Systems, State Key Laboratory for Mechanical Behaviour of Materials, School of Materials Science and Engineering, Xi'an Jiaotong University, Xi'an 710049, China. E-mail: tai.min@nju.edu.cn, taoli66@xjtu.edu.cn

^bSchool of Materials Science and Intelligent Engineering, Nanjing University, Suzhou 215163, China

[†]Electronic supplementary information (ESI) available. See DOI: <https://doi.org/10.1039/d5nr01908g>

[‡]These authors contributed equally to this work, and they should be viewed as first authors.

the crucial roles of polarization switching and ion migration in CIPS devices exhibiting dual-polarization states. However, the unique intrinsic multiple polarization states of CIPS-based electronic devices remain underexplored.

In this work, we fabricated two-terminal n^{++} -Si/CIPS/MoS₂ devices featuring CIPS as the functional layer. We investigated the characteristics of devices with intrinsic dual-polarization and quadruple-polarization of CIPS using switching scanning probe microscopy (SS-PFM)³¹ and conductive atomic force microscopy (C-AFM) techniques. The analysis revealed a memristive behaviour characterized by abrupt current jump correlated to voltage and frequency under positive bias in a dual-polarization CIPS/MoS₂ device. In contrast, the quadruple-polarization CIPS/MoS₂ device exhibited distinct rectification characteristics, achieving a switching ratio of approximately 10^4 . Our findings clearly elucidate the differences in the conduction mechanisms of FSJs based on dual- and quadruple-polarization states of CIPS, expanding the realm of CIPS for multifunctional electronic information systems.

Results and discussion

Fig. 1a displays the schematic diagram of an n^{++} -Si/CIPS/MoS₂ FSJ device, which consists of the semiconducting MoS₂ as the top electrode and n^{++} -Si as the bottom electrode. The Raman spectroscopy of CIPS in Fig. 1b presents the characteristic peaks of CIPS. The peaks identified near 70 cm⁻¹ and 315 cm⁻¹ are associated with cations In³⁺ and Cu⁺, while the peak at approximately 315 cm⁻¹ is attributed to structural distortions induced by the occupation of the S₆ octahedra by Cu⁺

ions. The peaks located near 102, 116, and 135 cm⁻¹ correspond to anionic (P₂S₆⁴⁻) vibrations. Furthermore, the peaks at 161, 263, and 374 cm⁻¹ correspond to the δ (S-P-P), δ (S-P-S), and ν (P-P) modes, respectively.^{32–34} The Raman results indicate the absence of IPS characteristic peaks (127 and 255 cm⁻¹)³³ in our CIPS films. Additionally, the Raman spectrum of MoS₂ exhibits two characteristic peaks at 382 cm⁻¹ and 408 cm⁻¹, corresponding to the E_{2g}¹ and A_{1g} that represent in-plane and out-of-plane vibrational modes,^{35,36} respectively, indicating the 2H phase of the MoS₂ flakes.³⁷ Based on previously reported Raman experimental data,³⁸ the MoS₂ in the relatively thick region was determined to be composed of four monolayers. Notably, the Raman spectrum of MoS₂ is influenced by the underlying CIPS layer,³⁹ resulting in a peak splitting at 374 cm⁻¹ and the emergence of minor peaks at 263 cm⁻¹, 303 cm⁻¹, and 315 cm⁻¹. In regions where MoS₂ is thin, the impact of the CIPS signal on the MoS₂ spectrum is more pronounced. Furthermore, a noticeable red shift in the A_{1g} peak of CIPS/MoS₂ regions suggests that these areas correspond to even thinner MoS₂ layers (fewer than four monolayers). The atomic structure of CIPS can be described as a sulfur atomic framework with octahedral voids occupied by Cu, In, and P-P pairs in sequence. Moreover, X-ray diffraction (XRD) characterization of the CIPS crystal indicates a single-crystalline nature, exhibiting a c-lattice parameter of about 13.04 Å (Fig. S1†).⁴⁰ Additionally, the high-resolution transmission electron microscopy (HR-TEM) revealed that our CIPS sample adheres to the trigonal crystal system *P*31c space group (Fig. S2†).⁴⁰ Fig. 1c presents the atomic force microscopy (AFM) morphology image of the CIPS/MoS₂ heterostructure, indicating a MoS₂ thickness of approximately 1.06 nm and a

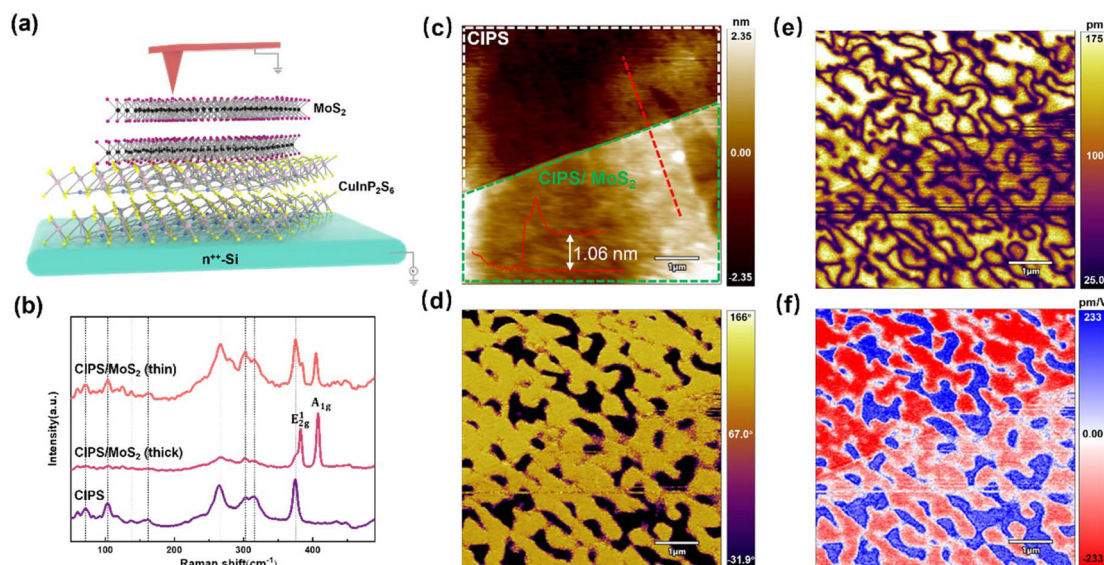


Fig. 1 Ferroelectric properties of as-prepared n^{++} -Si/CIPS/MoS₂ FSJ device. (a) Schematic structure of the FSJ device with C-AFM setup. (b) Raman spectra of the CIPS and the heterostructure. (c) AFM morphology of CIPS/MoS₂ heterostructure, the area of which is enclosed in a green polygon. The line profile shows that the thickness of MoS₂ is about 1.06 nm. PFM phase (d), amplitude (e), and piezoresponse (f) images reveal the pristine domain pattern of the device. The scale bar represents 1 μm.

CIPS thickness of 137 nm (Fig. S4†). Fig. 1d, e and f display the phase, amplitude, and piezoresponse images of CIPS that are partially covered by a MoS₂ flake, respectively measured by piezoresponse force microscopy (PFM). The MoS₂-covered CIPS still demonstrates a continuous domain pattern as that detected from the bare CIPS surface, albeit with reduced signal intensity. When CIPS is covered by an even thicker MoS₂ (~1.7 nm), much weaker amplitude and phase PFM signals were obtained (Fig. S5†).

Subsequently, SS-PFM measurements were conducted on the FSJ devices with dual-polarization states, revealing robust ferroelectric polarization switching in both the bare CIPS (Fig. 2a) and CIPS/MoS₂ regions (Fig. 2b). In Fig. 2a and b, a comparative analysis of the amplitude responses for bare CIPS and the CIPS/MoS₂ heterostructure is presented. Both configurations exhibit a more pronounced amplitude response under negative bias compared to that of positive bias. Notably, the CIPS/MoS₂ heterostructure demonstrates markedly enhanced cycle-to-cycle repeatability, indicating that the interfacial electrostatic effect can stabilize the polarization of CIPS. Moreover, the modulation of MoS₂ conductivity by CIPS polarization results in significant change in the coercive fields of the heterostructure. Specifically, when the CIPS polarization is oriented upward, the surface-bound positive charges induce electron doping in the adjacent MoS₂ layer, thereby promoting the accumulation of majority carriers and enhancing its conductivity. Conversely, when the polarization is reversed downward, the depletion of majority carriers in MoS₂ renders it rela-

tively insulating. Consequently, the coercive field V_{C1} (associated with the polarization switching from downward to upward) increases overall, whereas V_{C2} (polarization switching from upward to downward), undergoes an overall reduction, as evidenced in Fig. S7a and b.† Notably, an anomalous increase in V_{C2} is observed in the low bias range between 6 V and 7 V (Fig. S7b†). This phenomenon originates from the interfacial potential distribution effect arising from the non-piezoelectric nature of MoS₂—at low fields, the MoS₂ layer bears a considerable portion of the voltage drop, thereby reducing the effective field acting on CIPS. When the applied field reaches 8 V, the enhanced conductivity of MoS₂ diminishes its voltage division, enabling V_{C2} to revert to the theoretically predicted monotonic decrease. Additionally, the imprint effect in the CIPS/MoS₂ heterostructure is substantially reduced (Fig. S7d†). Statistical analysis of the hysteresis loops with and without MoS₂ coverage measured at different locations is presented in Fig. S7.† Furthermore, in CIPS/MoS₂ heterostructures with a MoS₂ thickness of 1.7 nm, SS-PFM measurements also exhibited similar reliable dual-state switching behaviour, but the signal intensity was reduced as expected (Fig. S8†).

As shown in Fig. 1a, an electric voltage was supplied between a conductive tip and the n⁺⁺-Si substrate for C-AFM measurements to probe the electrical transport characteristics of the FSJ device.^{23,41–43} Notably, since the work function of the metal tip is generally greater than that of MoS₂,⁴⁴ there exists a built-in electric field pointing from MoS₂ to the tip. Under positive bias, this built-in electric field is partially can-

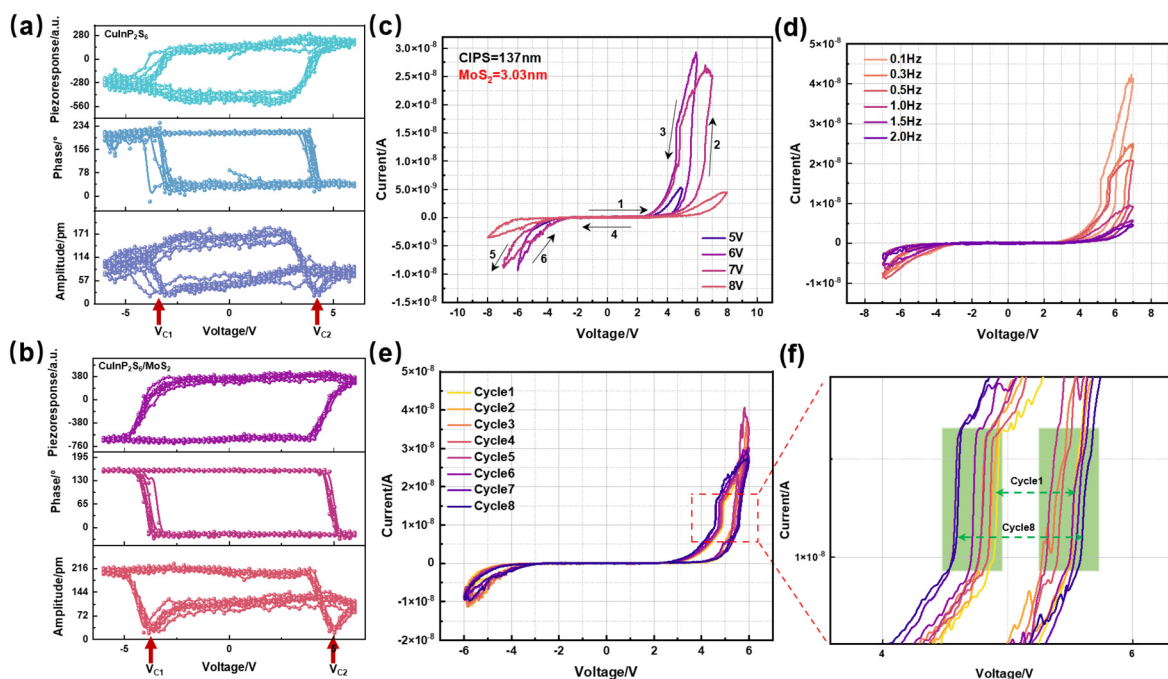


Fig. 2 Polarization switching behaviours and electrical characteristics of the n⁺⁺-Si/CIPS/MoS₂ FSJ device. (a) SS-PFM out-of-plane amplitude, phase, and piezoresponse hysteresis loop, revealing the dual-state ferroelectric switching of the CIPS. (b) Ferroelectric dual-state switching observed on the CIPS/MoS₂(1.06 nm) heterostructure. (c and d) *I*–*V* curves observed from the device under different voltage magnitudes and frequencies. (e) Multiple *I*–*V* sweep cycles under voltage sweep of ±6 V. (f) An enlarged view of the *I*–*V* curve in (e).

celed out, reducing the voltage drop at the junction. Conversely, under negative biases, the voltage drop at the junction increases. The applied voltage waveform is shown in Fig. S9,† wherein the triangular waveform is swept between 6 V and −6 V at a frequency of 0.5 Hz. As shown in Fig. 2c, the onset of electric conduction occurs when the sweeping voltage reaches approximately 5 V, with a measurable current of approximately 5 nA. The current–voltage (*I*–*V*) characteristics exhibited hysteresis at both positive and negative bias, demonstrating a continuously tunable resistance state.^{23,45} Furthermore, hysteresis was more pronounced under positive bias compared to negative bias, which may be attributed to the work function difference between CIPS and the MoS₂ and Si electrodes.^{23,46,47} When the window of the sweeping voltage is increased to 6 V and 7 V, substantial hysteresis was observed, suggesting a large-scale ionic displacement,⁴⁸ accompanied by a steep current jump when bias is gradually increased and a steep current drop in the reversed cycle. The sudden change of current indicates the presence of a threshold voltage, where the Cu⁺ ions may undergo coherent hopping or migration collectively due to a possible energy barrier for Cu⁺ migration. Subsequently, under even higher sweeping voltages (±8 V), only minimal hysteresis remains, probably due to the irreversible depletion of Cu⁺ ions that are trapped at the interfaces.

Fig. 2d presents the *I*–*V* loops as a function of frequency at a fixed sweep voltage of ±7 V. It is evident that the current jump accompanied by prominent hysteresis occurred only at frequencies below 0.5 Hz, suggesting that the behaviour should be attributed to collective moments of the Cu⁺ ions when the frequency of the voltage variation is slow enough. This observation can be attributed to the diminished lag in Cu⁺ ion migration in response to the external electric field at lower frequencies. As shown in Fig. 2e, the current jump is consistently observed in repeated cycling. Notably, the magnified section highlighted by the green region (Fig. 2f) reveals that, with an increasing number of cycles, the hysteresis window gradually expands. Such expansion may be due to trapped ions or a slowdown of the ionic diffusion upon cycling.²⁴

Furthermore, we studied the *I*–*V* characteristics depending on different thicknesses (3.03 nm, 2.13 nm, and 1.61 nm) of MoS₂ in the FSJ devices (Fig. S10†), with varied bias window (±5 ~ ±9 V) and sweeping frequency (0.1–0.5 Hz). By plotting the logarithm of the current, we further demonstrate that the hysteresis loop in the *I*–*V* loops is governed predominantly by ferroelectric polarization switching.²⁰ Generally, these samples exhibit the same trend of the *I*–*V* characteristics as those illustrated in Fig. 2, but the thickness of MoS₂ significantly influences the voltage at which the current jumps manifest. Under the fixed sweeping frequency, FSJ with thicker MoS₂ (3.03 nm) start to exhibit the current jump when the bias window is ±6 V and ±7 V. When it further increases to ±8 V and ±9 V, the current jump disappears, and the *I*–*V* characteristics exhibit hysteresis analogous to that observed at ±5 V. In contrast, FSJ with thinner MoS₂ (2.13 nm and 1.61 nm) start to exhibit current jumps at a smaller bias window (±5 V) and persist

until ±7 V. This behaviour can be attributed to the enhanced conductivity of thinner MoS₂,⁴⁹ which facilitates more rapid aggregation and migration of Cu⁺ ions at lower voltages. Under a large sweeping bias window (e.g., ±9 V), the concentration of free Cu⁺ ions can be reduced due to certain irreversible charge trapping,^{24,50} leading to only minimal migration at elevated voltages and resulting in a gradual decline in current. In addition, the FSJ device with the thinnest MoS₂ (1.63 nm) has the largest on/off ratio, the maximum of which can reach 2.7×10^3 when the bias window and sweeping frequency are ±6 V and 0.1 Hz, respectively. Another MoS₂ thickness-dependent observation is that the width of the hysteresis window gradually expands with reduced MoS₂ thickness, which may be attributed to its enhanced conductivity,⁴⁹ thereby enabling more extensive Cu⁺ ion migration.

Remarkably, ferroelectric hysteresis demonstrating robust quadruple polarization states was successfully obtained on a different CIPS (65 nm)/MoS₂ (4.56 nm) FSJ device, the domain pattern of which is provided in Fig. S11.† Compared to the bare CIPS (Fig. 3a), the hysteresis loops obtained through the MoS₂ flake have better repeatability and persistent four distinct coercive biases associated with the quadruple polarization states. Complementary evidence for the existence of quadruple polarization states under different bias windows is provided in Fig. S12.† A significant change is the reduction of *V*_{C3} with MoS₂ coverage (Fig. 3b), which corresponds to the regular polarization transition from the downward to the upward state in CIPS in the same direction as the externally applied voltage. Compared to the local ferroelectric hysteresis loops obtained using the tip as the top electrode on the bare CIPS surface, the MoS₂ electrode offers broader coverage and facilitates the polarization reversal, thereby contributing to the reduction in *V*_{C3}. The distribution of four coercive fields, measured over multiple cycles at various bias levels in both bare CIPS and CIPS/MoS₂ regions, is statistically analysed and shown in Fig. S13.† The analysis demonstrates that MoS₂ underscores its pivotal role in modulating polarization dynamics.

The C-AFM measurements of the quadruple-polarization state FSJ demonstrate dramatically different *I*–*V* characteristics compared to the dual-state FSJ, exhibiting highly rectifying behaviour across the device (Fig. 3c). High conduction current is still observed under positive bias, reaching the microampere range, whereas high resistance persists over the entire negative bias range, with current restricted to the sub-nanoampere scale. A maximum rectification ratio of up to 2.5×10^4 can be achieved, an order of magnitude higher than that of the dual-polarization state FSJ. Furthermore, at lower frequencies (e.g., 0.3 Hz and 0.1 Hz), the opening of the hysteresis is largely increased under positive bias but exerts a negligible effect under negative bias (Fig. 3d) due to the same reason as explained before. The *I*–*V* characteristics also exhibit robust reproducibility over 12 cycles (Fig. 3e). Fig. 3f provides a magnified view of the hysteresis crossover observed under positive bias in the *I*–*V* characteristics. The detailed correlation between the representative piezoresponse hysteresis loop and

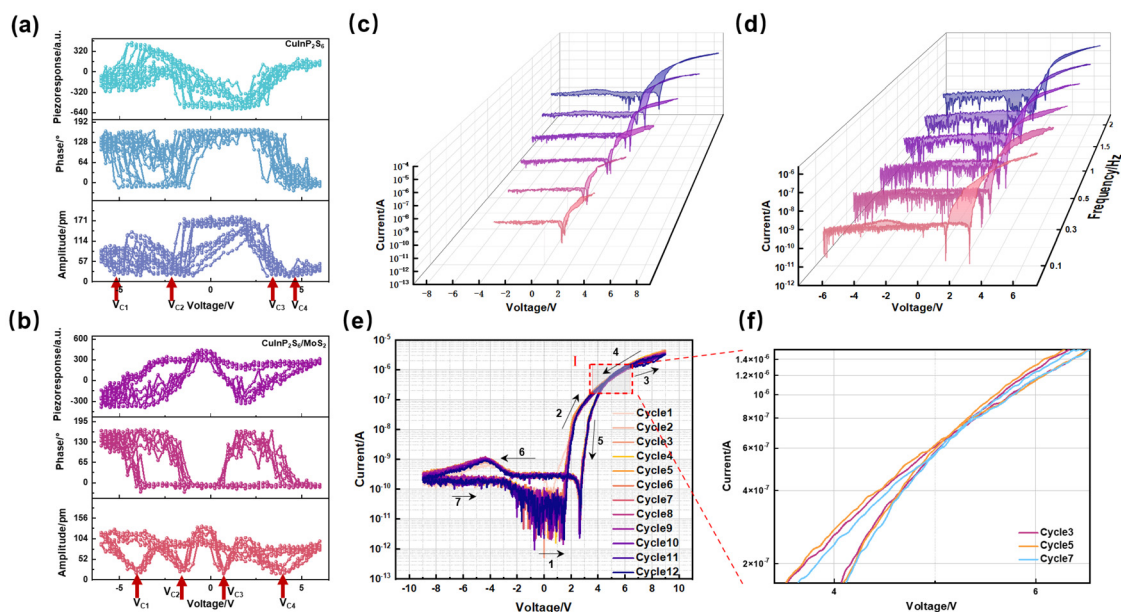


Fig. 3 Ferroelectric property and electrical characteristics of the vdW FSJ. (a) Out-of-plane SS-PFM amplitude, phase, and piezoresponse hysteresis loop, revealing the quadruple ferroelectric switching of the CIPS. (b) Robust ferroelectric quadruple switching was still observed on the CIPS/MoS₂ heterostructure. (c) Response of I - V curves to different voltages. (d) I - V characteristics of the device at 7 V as a function of frequency. (e) Consecutive 12 sweep cycles are conducted with $V_{\text{max}} = 9.0$ V. (f) Enlarged sections labelled I within the curve presented in (e).

the corresponding I - V characteristics of the device within a bias window of ± 8 V is presented in Fig. S14.† With increasing positive bias, the ferroelectric polarization undergoes its first switching 2.9 V (V_{C3}), manifesting as a transition from a high-resistance state (HRS) to a low-resistance state (LRS) in the I - V characteristics. The V_{C3} directly corresponds to the voltage where the I - V curve slope changes under positive bias. With further increasing of positive voltage, ferroelectric switching occurs again in the direction against the applied electric field at 4.8 V (V_{C4}), resulting in a hysteresis crossover of the I - V curve at approximately the same voltage. Subsequently, the device transitions back to the HRS upon the polarity reversal of the applied voltage. As the negative bias increases, the ferroelectric polarization undergoes another switching event at -1.2 V (V_{C2}), but such switching is not discernible in the I - V curve. This absence is likely due to the diminished polarization strengths at V_{C2} , as further elucidated in Fig. 4, leading to a minimal effect on the device's transport characteristics. With further increases in negative bias, an additional polarization switching occurs at -3.4 V (V_{C1}), leading to a small bump in the negative bias region of the I - V curve.

Fig. 4a and b illustrate the proposed mechanism underlying the intrinsic dual-polarization states in the n^{++} -Si/CIPS/MoS₂ device, wherein Cu^+ ions and electrons jointly contribute to electronic transport behaviors. When a positive voltage is applied to the bottom n^{++} -Si substrate, Cu^+ ions migrate toward the MoS₂, forming localized conductive pathways. The localized accumulation of Cu^+ ions near the MoS₂ interface generates a Cu^+ -rich region, effectively reducing the interfacial contact barrier at the CIPS/MoS₂ junction.^{23,51} This reduction facilitates further long-range Cu^+ migration, as evidenced by

the significantly higher current under positive bias in Fig. 2c. Conversely, applying a negative voltage to the substrate drives Cu^+ ions away from the MoS₂ interface, creating a Cu^+ depleted region. This depletion increases the contact barrier at the CIPS/MoS₂ junction and inhibits long-range Cu^+ transport, leading to reduced current and a diminished hysteresis loop under negative bias.

For n^{++} -Si/CIPS/MoS₂ FSJs exhibiting intrinsic quadruple-polarization states, the underlying mechanism of ion migration remains applicable but requires a more nuanced explanation to delineate the specific influence of ion dynamics on the polarization behavior of CIPS. Inspired by the concept of AFE/FE domain blocks,²¹ a simplified dual-domain block model is employed to represent the quadruple polarization states of CIPS. As shown in Fig. 4c-g, the polarization state of each layer is intended to capture the net polarization across multiple layers within the actual CIPS material. The ground state polarization configuration of CIPS in the quadruple-polarization state of the FTJ is illustrated in Fig. 4c. The topmost and bottommost regions exhibit a head-to-head alignment with the ferroelectric (FE) domain in each monolayer, while the intermediate layers adopt an antiferroelectric (AFE) configuration, corresponding to the energetically most stable state.²¹

Upon applying a small positive voltage to the substrate, Cu^+ ions within the regions adjacent to the n^{++} -Si electrode undergo migration across the vdW gap,^{22,52,53} triggering a local reversal of polarization, as indicated by the migration pathway depicted in Fig. S15a.† In contrast, the regions farther from the substrate experience a significantly reduced electric field, insufficient to facilitate complete polarization switching

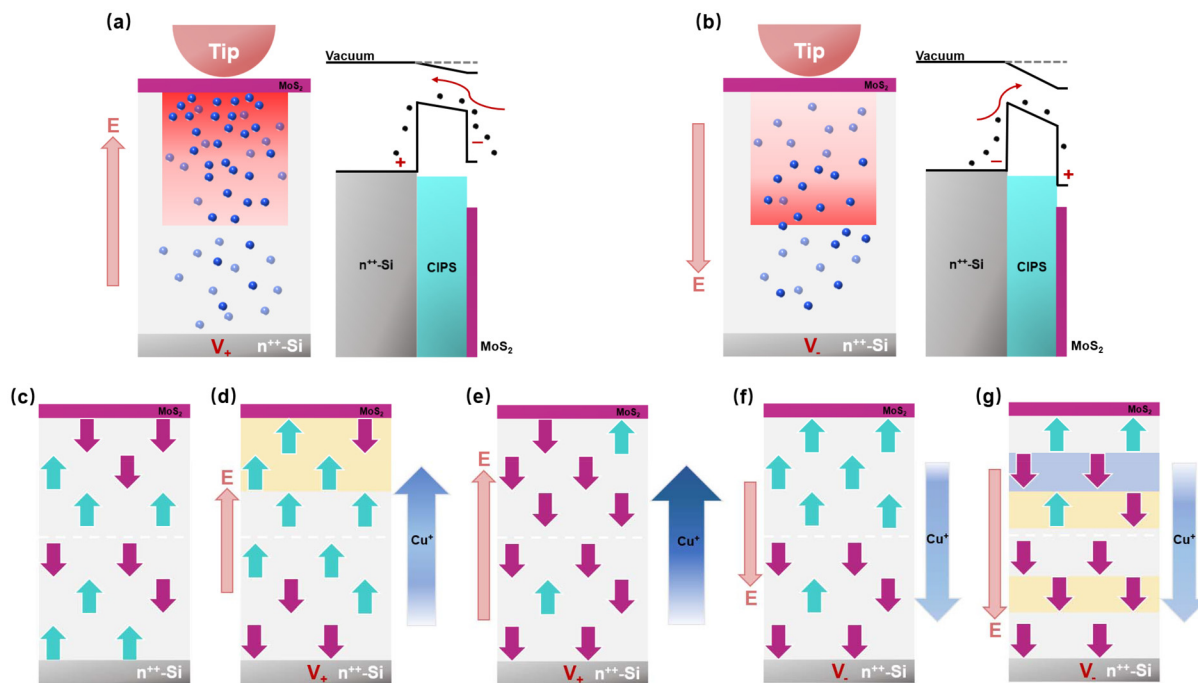


Fig. 4 Schematic representation of the mechanism by which Cu^+ migration under positive and negative bias influences the electrical transport characteristics of FSJ devices. (a and b) Energy band diagrams illustrating the Cu^+ ion migration (blue spheres) and electron distribution (black spheres) in the FSJ device under positive and negative bias conditions, respectively. (c) Ground-state polarization configuration of the FSJ exhibiting an intrinsic quadruple-polarization state. (d) Polarization configuration of the FSJ device under a low positive bias, exhibiting a net polarization of $2P_{\uparrow}$. Regions undergoing HL-switching are indicated by orange-highlighted areas. (e) Polarization configuration under a high positive bias, demonstrating a net polarization of $4P_{\uparrow}$. (f) Polarization configuration under a low negative bias, with a net polarization of $1P_{\uparrow}$. (g) Polarization configuration under a high negative bias, showing a net polarization of $3P_{\downarrow}$.

in each monolayer. Consequently, only half-layer-by-half-layer switching (HL-switching) occurs,²¹ following the trajectory illustrated in Fig. S15b.† The regions undergoing HL-switching are delineated by the yellow-highlighted areas in Fig. 4. The resultant polarization configuration is presented in Fig. 4d, wherein the net polarization of CIPS is relatively weak. This diminished polarization strength fails to produce discernible features in the I - V characteristics of the device, further substantiating the intricate interplay between local ionic motion and the correlated polarization states.

As the positive voltage increases, significant interlayer Cu^+ migration occurs, crossing the vdW gaps. As illustrated in Fig. 4e, the polarization configuration in the region immediately adjacent to the substrate may stabilize due to Cu^+ depletion, rendering the layer immobile. All remaining regions undergo Cu^+ migration, leading to polarization reversal across multiple layers and a substantial increase in net polarization. This enhanced polarization can be responsible for the crossing point observed in the I - V curve in Fig. 3e. Under the reverse bias, at low negative voltages, Cu^+ migration across the vdW gap is confined to regions near the MoS_2 interface, inducing localized polarization reversal (Fig. 4f). Consequently, the net polarization remains relatively weak. At higher negative voltages, Cu^+ migration occurs in the finite region (as delineated by the blue-highlighted area in Fig. 4g), inducing further polar-

ization reversal. However, the depletion of Cu^+ ions further enhances the local barrier⁵¹ in addition to the initial potential barriers, thereby impeding the penetration of the electric field.⁵⁴ Consequently, HL-switching is restricted to regions slightly further from the MoS_2 interface (Fig. 4f), resulting in a moderately enhanced net polarization and influencing the I - V characteristics as observed in Fig. 3f. The directional migration of Cu^+ ions dynamically modulates the contact barrier at the CIPS/ MoS_2 interface, either promoting or inhibiting further ionic transport. Conversely, the interplay between interlayer Cu^+ migration and intralayer hopping under varying electric fields governs the polarization dynamics of CIPS, particularly in systems exhibiting intrinsic multiple polarization states. These coupled processes collectively manifest as distinct I - V characteristics, demonstrating the intricate interaction between ionic transport and ferroelectric polarization in this heterostructure.

Conclusions

In summary, this work provides a comprehensive investigation into the coupling mechanisms of ionic migration and ferroelectric polarization switching in $n^{++}\text{-Si/CIPS/MoS}_2$ FSJ, emphasizing their dependence on MoS_2 thickness, frequency, and

magnitude of the externally applied biases. Through detailed analysis, we demonstrate that thinner MoS₂ layers significantly enhance electric transport performance by facilitating Cu⁺ migration and modulating interfacial barrier dynamics, thereby promoting long-range ionic transport. Furthermore, the discovery of intrinsic quadruple-polarization states in CIPS underscores the unique multi-state configurations of its ferroelectric and antiferroelectric domains. These configurations arise from complex interactions between interlayer ionic migration and intralayer hopping, which exhibit distinct electrical transport signatures under varying bias conditions. The devices display moderate switching ratios, stability against frequency variations, and reproducible hysteresis behaviour, establishing their potential for non-volatile memory applications. Future efforts can focus on refining interfacial engineering and leveraging these mechanisms to achieve higher device integration and multifunctionality, thereby advancing the application of intrinsic multi-state FSJ in high-performance memory, logic, and neuromorphic computing technologies.

Experimental section

Device fabrication

Single-crystalline CIPS crystals were synthesized *via* the chemical vapor transport (CVT) method. The synthesis involved maintaining the source zone and growth zone temperatures at 750 °C and 650 °C, respectively. After a 7 day reaction period under these conditions, followed by natural cooling to room temperature, greenish-yellow crystals were successfully obtained. The as-grown CIPS crystals were transferred onto an n⁺⁺-Si substrate *via* mechanical exfoliation. Separately, MoS₂ was exfoliated onto a polydimethylsiloxane (PDMS) substrate. Using a two-dimensional transfer platform, the MoS₂ flake was precisely aligned with the CIPS layer and stacked to form a heterojunction structure.

Material characterization

The crystal structure of CIPS was characterized using X-ray diffraction (XRD) analysis (D/MAX-2400, Rigaku, Japan). A Cu radiation source was utilized, and the diffraction patterns were recorded over a 2θ range of 10° to 80° at a scanning speed of 5° min⁻¹. The Raman spectra of the Si/CIPS/MoS₂ heterostructure were measured under excitation from a 532 nm wavelength laser source. The TEM analysis was performed using an FEI Titan 60–300 microscope equipped with a monochromator and operated at an accelerating voltage of 300 kV. The lens aberrations were controlled as follows: two-fold astigmatism (A1) < 5 nm, three-fold astigmatism (A2) < 20 nm, and axial coma (B2) < 10 nm. High-resolution TEM (HR-TEM) images were captured using a Gatan Oneview camera with a 4k × 4k resolution. To minimize ion-beam damage during the initial focused ion beam (FIB) preparation process, the samples were pre-coated with protective Pt layers prior to TEM measurements.

Piezoresponse force microscopy (PFM)

PFM was performed on the fabricated CIPS/MoS₂ heterojunction using a commercial atomic force microscope (MFP-3D, Oxford Instruments, USA) under ambient conditions. The Dual AC Resonance Tracking (DART) mode was employed to improve the signal-to-noise ratio and minimize topographic crosstalk.⁵⁵ Signal detection was carried out using Pt/Ir-coated conductive probes (PPP-EFM, Nanosensors, Netherlands) with a nominal spring constant of ~3 N m⁻¹ and a free resonance frequency of approximately 75 kHz. AC voltages in the range of 0.3–0.5 V_{AC} were applied to the samples *via* the conductive probe at the tip-sample contact resonance frequency (~350 kHz). The tip had a nominal radius of curvature of ~30 nm. Calibration of the cantilever spring constant and photo-detector sensitivity was conducted using the Sader and thermal noise methods.⁵⁶ The raw amplitude and phase data were fitted using a simple harmonic oscillator model to derive the quantitative piezoresponse values.⁵⁷ The localized hysteresis loops of CIPS and the heterojunction were acquired using the Switching Spectroscopy PFM (SS-PFM) mode with the same PFM tip employed for imaging. The DC pulse width was set to 20 ms, with a fixed rise time of 0.5 ms for each pulse. To ensure that the polarization states were not altered by the AC detection voltage, a low detection voltage (V_{AC}) in the range of 0.3–0.5 V was used to monitor the piezoresponse signal both during and after each DC pulse, thereby guaranteeing the reliability of the collected data. To minimize ambiguity arising from electrostatic forces during on-field (V_{DC} applied) measurements, we primarily analysed off-field (remanent) data. Multiple hysteresis loops were recorded at each location to ensure data consistency.

Conductive atomic force microscopy measurements

Single-point current-voltage (*I*-*V*) measurements were conducted using the ORCA module integrated into a commercial atomic force microscope. The voltage was applied to the conducting n⁺⁺-Si bottom electrode, which was continuously swept while the current was simultaneously recorded. A conductive Pt/Si cantilever tip was used to probe the sample surface. All *I*-*V* measurements were performed under ambient temperature conditions to ensure reproducibility and reliability.

Author contributions

J. Liu performed the experiments and wrote the manuscript. H. Feng helped with experiments and data analysis. Y. Wu advised on the CVT and PFM experiments. Y. Li provided help with writing the manuscript. Q. Wang and F. Hou advised on data analysis. T. Min and T. Li conceived the idea and supervised the research.

Conflicts of interest

The authors declare no conflicts of interest.

Data availability

The data supporting this article have been included as part of the ESI.†

Acknowledgements

This work was financially supported by the National Key R&D Program of China (Grant No. 2021YFA1202200).

References

- 1 A. Sebastian, M. Le Gallo, R. Khaddam-Aljameh and E. Eleftheriou, *Nat. Nanotechnol.*, 2020, **15**, 529–544.
- 2 J. Yu, Y. Wang, S. Qin, G. Gao, C. Xu, Z. L. Wang and Q. Sun, *Mater. Today*, 2022, **60**, 158–182.
- 3 F. Cai, J. M. Correll, S. H. Lee, Y. Lim, V. Bothra, Z. Zhang, M. P. Flynn and W. D. Lu, *Nat. Electron.*, 2019, **2**, 290–299.
- 4 M. Si, Y. Luo, W. Chung, H. Bae, D. Zheng, J. Li, J. Qin, G. Qiu, S. Yu and P. D. Ye, A Novel Scalable Energy-Efficient Synaptic Device: Crossbar Ferroelectric Semiconductor Junction, IEEE International Electron Devices Meeting, San Francisco, 2019.
- 5 M. Si, Z. Zhang, S.-C. Chang, N. Haratipour, D. Zheng, J. Li, U. E. Avcı and P. D. Ye, *ACS Nano*, 2021, **15**, 5689–5695.
- 6 J. Wu, H.-Y. Chen, N. Yang, J. Cao, X. Yan, F. Liu, Q. Sun, X. Ling, J. Guo and H. Wang, *Nat. Electron.*, 2020, **3**, 466–472.
- 7 Y. Liu, Y. Wu, H. Han, Y. Wang, R. Peng, K. Liu, D. Yi, C.-W. Nan and J. Ma, *Adv. Funct. Mater.*, 2024, **34**, 2306945.
- 8 J. Gong, Y. Wei, Y. Wang, Z. Feng, J. Yu, L. Cheng, M. Chen, L. Li, Z. L. Wang and Q. Sun, *Adv. Funct. Mater.*, 2024, **34**, 2408435.
- 9 S. Seo, J.-J. Lee, R.-G. Lee, T. H. Kim, S. Park, S. Jung, H.-K. Lee, M. Andreev, K.-B. Lee, K.-S. Jung, S. Oh, H.-J. Lee, K. S. Kim, G. Y. Yeom, Y.-H. Kim and J.-H. Park, *Adv. Mater.*, 2021, **33**, 2102980.
- 10 F. Guo, M. Song, M.-C. Wong, R. Ding, W. F. Io, S.-Y. Pang, W. Jie and J. Hao, *Adv. Funct. Mater.*, 2022, **32**, 2108014.
- 11 J. R. Wallbank, D. Ghazaryan, A. Misra, Y. Cao, J. S. Tu, B. A. Piot, M. Potemski, S. Pezzini, S. Wiedmann, U. Zeitler, T. L. M. Lane, S. V. Morozov, M. T. Greenaway, L. Eaves, A. K. Geim, V. I. Fal'ko, K. S. Novoselov and A. Mishchenko, *Science*, 2016, **353**, 575–579.
- 12 J. C. W. Song and N. M. Gabor, *Nat. Nanotechnol.*, 2018, **13**, 986–993.
- 13 A. J. Healey, S. C. Scholten, T. Yang, J. A. Scott, G. J. Abrahams, I. O. Robertson, X. F. Hou, Y. F. Guo, S. Rahman, Y. Lu, M. Kianinia, I. Aharonovich and J. P. Tetienne, *Nat. Phys.*, 2023, **19**, 87–91.
- 14 S. Seo, S.-H. Jo, S. Kim, J. Shim, S. Oh, J.-H. Kim, K. Heo, J.-W. Choi, C. Choi, S. Oh, D. Kuzum, H. S. P. Wong and J.-H. Park, *Nat. Commun.*, 2018, **9**, 5106.
- 15 M.-K. Kim and J.-S. Lee, *Nano Lett.*, 2019, **19**, 2044–2050.
- 16 T. Zhang, X. Guo, P. Wang, X. Fan, Z. Wang, Y. Tong, D. Wang, L. Tong and L. Li, *Nat. Commun.*, 2024, **15**, 2471.
- 17 A. N. Morozovska, E. A. Eliseev, N. V. Morozovsky and S. V. Kalinin, *Phys. Rev. B*, 2017, **95**, 195413.
- 18 S. M. Yang, A. N. Morozovska, R. Kumar, E. A. Eliseev, Y. Cao, L. Mazet, N. Balke, S. Jesse, R. K. Vasudevan, C. Dubourdieu and S. V. Kalinin, *Nat. Phys.*, 2017, **13**, 812–818.
- 19 Z. Zhong, S. Wu, X. Li, Z. Wang, Q. Yang, B. Huang, Y. Chen, X. Wang, T. Lin, H. Shen, X. Meng, M. Wang, W. Shi, J. Wang, J. Chu and H. Huang, *ACS Nano*, 2023, **17**, 12563–12572.
- 20 J. Zhou, A. Chen, Y. Zhang, D. Pu, B. Qiao, J. Hu, H. Li, S. Zhong, R. Zhao, F. Xue, Y. Xu, K. P. Loh, H. Wang and B. Yu, *Adv. Mater.*, 2023, **35**, 2302419.
- 21 T. Li, Y. Wu, G. Yu, S. Li, Y. Ren, Y. Liu, J. Liu, H. Feng, Yu Deng, M. Chen, Z. Zhang and T. Min, *Nat. Commun.*, 2024, **15**, 2653.
- 22 J. A. Brehm, S. M. Neumayer, L. Tao, A. O'Hara, M. Chyasnachichus, M. A. Susner, M. A. McGuire, S. V. Kalinin, S. Jesse, P. Ganesh, S. T. Pantelides, P. Maksymovych and N. Balke, *Nat. Mater.*, 2020, **19**, 43–48.
- 23 X. Jiang, X. Wang, X. Wang, X. Zhang, R. Niu, J. Deng, S. Xu, Y. Lun, Y. Liu, T. Xia, J. Lu and J. Hong, *Nat. Commun.*, 2022, **13**, 574.
- 24 P. Li, A. Chaturvedi, H. Zhou, G. Zhang, Q. Li, J. Xue, Z. Zhou, S. Wang, K. Zhou, Y. Weng, F. Zheng, Z. Shi, E. H. T. Teo, L. Fang and L. You, *Adv. Funct. Mater.*, 2022, **32**, 2201359.
- 25 Y. Xia, N. Lin, J. Zha, H. Huang, Y. Zhang, H. Liu, J. Tong, S. Xu, P. Yang, H. Wang, L. Zheng, Z. Zhang, Z. Yang, Y. Chen, H. P. Chan, Z. Wang and C. Tan, *Adv. Mater.*, 2024, **36**, 2403785.
- 26 Y. Liu, Y. Wu, B. Wang, H. Chen, D. Yi, K. Liu, C.-W. Nan and J. Ma, *Nano Res.*, 2023, **16**, 10191–10197.
- 27 B. Li, S. Li, H. Wang, L. Chen, L. Liu, X. Feng, Y. Li, J. Chen, X. Gong and K.-W. Ang, *Adv. Electron. Mater.*, 2020, **6**, 2000760.
- 28 W. Ci, P. Wang, W. Xue, H. Yuan and X. Xu, *Adv. Funct. Mater.*, 2024, **34**, 2316360.
- 29 Y. Wang, W. Li, Y. Guo, X. Huang, Z. Luo, S. Wu, H. Wang, J. Chen, X. Li, X. Zhan and H. Wang, *J. Mater. Sci. Technol.*, 2022, **128**, 239–244.
- 30 Z. Shang, L. Liu, G. Wang, H. Xu, Y. Cui, J. Deng, Z. Lou, Y. Yan, J. Deng, S.-T. Han, T. Zhai, X. Wang, L. Wang and X. Wang, *ACS Nano*, 2024, **18**, 30530–30539.
- 31 S. Jesse, A. P. Baddorf and S. V. Kalinin, *Appl. Phys. Lett.*, 2006, **88**, 062908.
- 32 M. Si, P.-Y. Liao, G. Qiu, Y. Duan and P. D. Ye, *ACS Nano*, 2018, **12**, 6700–6705.
- 33 R. Rao, R. Selhorst, B. S. Conner and M. A. Susner, *Phys. Rev. Mater.*, 2022, **6**, 045001.
- 34 Y. Sun, R. Zhang, C. Teng, J. Tan, Z. Zhang, S. Li, J. Wang, S. Zhao, W. Chen, B. Liu and H.-M. Cheng, *Mater. Today*, 2023, **66**, 9–16.
- 35 S. Najmaei, Z. Liu, P. M. Ajayan and J. Lou, *Appl. Phys. Lett.*, 2012, **100**, 013106.

- 36 G. Plechinger, S. Heydrich, J. Eroms, D. Weiss, C. Schüller and T. Korn, *Appl. Phys. Lett.*, 2012, **101**, 101906.
- 37 Y. Sun, S. Yin, R. Peng, J. Liang, X. Cong, Y. Li, C. Li, B. Wang, M. L. Lin, P. H. Tan, C. Wan and K. Liu, *Nano Lett.*, 2023, **23**, 5342–5349.
- 38 B. Chakraborty, H. S. S. R. Matte, A. K. Sood and C. N. R. Rao, *J. Raman Spectrosc.*, 2013, **44**, 92–96.
- 39 J. Cheng, J.-H. Yuan, P. Y. Li, J. Wang, Y. Wang, Y. W. Zhang, Y. Zheng and P. Zhang, *ACS Appl. Mater. Interfaces*, 2024, **16**, 24987–24998.
- 40 J. Deng, Y. Liu, M. Li, S. Xu, Y. Lun, P. Lv, T. Xia, P. Gao, X. Wang and J. Hong, *Small*, 2020, **16**, e1904529.
- 41 Q. Chen, G. Liu, W. Xue, J. Shang, S. Gao, X. Yi, Y. Lu, X. Chen, M. Tang, X. Zheng and R.-W. Li, *ACS Appl. Electron. Mater.*, 2019, **1**, 789–798.
- 42 D. Berco, Y. Zhou, S. R. Gollu, P. S. Kalaga, A. Kole, M. Hassan and D. S. Ang, *ACS Nano*, 2018, **12**, 5946–5955.
- 43 S. Eom, P. Kavle, D. Kang, Y. Kim, L. W. Martin and S. Hong, *Adv. Funct. Mater.*, 2024, 2406944.
- 44 S. Walia, S. Balendhran, Y. Wang, R. A. Kadir, A. S. Zoofakar, P. Atkin, J. Z. Ou, S. Sriram, K. Kalantar-zadeh and M. Bhaskaran, *Appl. Phys. Lett.*, 2013, **103**, 232105.
- 45 X. Wang, Z. Shang, C. Zhang, J. Kang, T. Liu, X. Wang, S. Chen, H. Liu, W. Tang, Y.-J. Zeng, J. Guo, Z. Cheng, L. Liu, D. Pan, S. Tong, B. Wu, Y. Xie, G. Wang, J. Deng, T. Zhai, H.-X. Deng, J. Hong and J. Zhao, *Nat. Commun.*, 2023, **14**, 840.
- 46 C. H. Yang, J. Seidel, S. Y. Kim, P. B. Rossen, P. Yu, M. Gajek, Y. H. Chu, L. W. Martin, M. B. Holcomb, Q. He, P. Maksymovych, N. Balke, S. V. Kalinin, A. P. Baddorf, S. R. Basu, M. L. Scullin and R. Ramesh, *Nat. Mater.*, 2009, **8**, 485–493.
- 47 T. Choi, S. Lee, Y. J. Choi, V. Kiryukhin and S.-W. Cheong, *Science*, 2009, **324**, 63–66.
- 48 N. Balke, S. M. Neumayer, J. A. Brehm, M. A. Susner, B. J. Rodriguez, S. Jesse, S. V. Kalinin, S. T. Pantelides, M. A. McGuire and P. Maksymovych, *ACS Appl. Mater. Interfaces*, 2018, **10**, 27188–27194.
- 49 T. H. Ly, J. Zhao, H. Kim, G. H. Han, H. Nam and Y. H. Lee, *Adv. Mater.*, 2016, **28**, 7723–7728.
- 50 Y. Xia, N. Lin, J. Zha, H. Huang, Y. Zhang, H. Liu, J. Tong, S. Xu, P. Yang, H. Wang, L. Zheng, Z. Zhang, Z. Yang, Y. Chen, H. P. Chan, Z. Wang and C. Tan, *Adv. Mater.*, 2024, 2403785.
- 51 Y. Huang, S. Yao, F. Sun, X. Zhang, W. Chen, X. Liu and Y. Zheng, *ACS Appl. Electron. Mater.*, 2023, **5**, 5625–5632.
- 52 S. M. Neumayer, L. Tao, A. O'Hara, J. Brehm, M. Si, P.-Y. Liao, T. Feng, S. V. Kalinin, P. D. Ye, S. T. Pantelides, P. Maksymovych and N. Balke, *Phys. Rev. Appl.*, 2020, **13**, 064063.
- 53 D. Zhang, P. Schoenherr, P. Sharma and J. Seidel, *Nat. Rev. Mater.*, 2023, **8**, 25–40.
- 54 X. Jiang, X. Zhang, Z. Deng, J. Deng, X. Wang, X. Wang and W. Yang, *Nat. Commun.*, 2024, **15**, 10822.
- 55 B. J. Rodriguez, C. Callahan, S. V. Kalinin and R. Proksch, *Nanotechnology*, 2007, **18**, 475504.
- 56 M. J. Higgins, R. Proksch, J. E. Sader, M. Polcik, S. Mc Endoo, J. P. Cleveland and S. P. Jarvis, *Rev. Sci. Instrum.*, 2006, **77**, 013701.
- 57 A. Gannepalli, D. G. Yablon, A. H. Tsou and R. Proksch, *Nanotechnology*, 2011, **22**, 355705.